

Silicon Sensor Irradiation Studies for the LHC HL Upgrade



BROWN

Andrew Thomas Kent

Department of Physics
Brown University

Submitted in partial satisfaction of the requirements for the
Degree of Master of Science
in Physics

Advisor: Professor Ulrich Heintz

May 2022

© 2022 - Andrew Thomas Kent

All rights reserved.

*This thesis by Andrew Thomas Kent is accepted in its present form by the
Department of Physics as satisfying the thesis requirement for the degree of Master
of Science.*

.....
Date Ulrich Heintz, Advisor

Recommended to the Graduate Council

.....
Date Andrew G. Campbell, Dean of the Graduate School

This work is dedicated to my parents, Zaida Soriano and Ron Kent.

Acknowledgements

I am very grateful to have had many people help me along the way in my pursuit of an education in physics, and I especially wanted acknowledge a few of those who especially helped me with my goals.

Before arriving at Brown University I received extensive mentoring from Distinguished Professor of Physics at UCLA, George Morales - we would meet every week for a few hours and he would teach me what it meant to be a theoretical physicist and how one should go about solving very difficult problems. I will always look back fondly on those meetings I had with him.

While at UCLA I was the recipient of the Nicholas Dieter Memorial Scholarship which was awarded by former U.S. Ambassador Robert J. Dieter and Mrs. Gwynneth Dieter, their kind words and support helped me quell many doubts I had about the future.

I would like to thank Professor Ulrich Heintz for allowing me to learn in his lab as a laboratory assistant and also for his guidance in writing this thesis, my time working in his lab has been a wonderful education.

Also, from the Brown University Silicon Lab I would like to whole heartedly thank Eric Spencer and Nick Hinton. Eric taught me almost all of the techniques and skills I used in my research presented in this thesis, and I am very grateful for all his support.

Finally, I would like to thanks my family, friends, my girlfriend Yasemin Kirac and most especially my mother. At every step of the way she has supported me. When I decided to switch my path from cooking professionally to going back to school and pursuing physics she was my number one fan, and for that and an incomprehensible list of other supportive things she has done for me, I am eternally grateful.

Abstract

Hello, this is my abstract

Table of Contents

Dedication	iii
Acknowledgements	iv
Abstract	v
1 Introduction	1
1.1 The Large Hadron Collider	1
1.1.1 The High-Luminosity Large Hadron Collider (HL-LHC)	1
1.2 The Compact Muon Solenoid Experiment at CERN	3
1.2.1 Silicon Sensors	4
1.2.1.1 Pixel Detectors	4
1.2.1.2 Strip Sensors	4
2 Silicon Detectors	5
2.1 Silicon Sensor Properties	5
2.1.1 PN Junction	6
3 Radiation Damage	11
3.1 Bulk Silicon Damage	11
3.2 Non-Ionizing-Energy-Loss (NEIL) Hypothesis	12
3.3 Characterizing Fluence (Φ_{eq})	14
3.3.1 Leakage Current	14
3.3.2 Effective Doping Concentration N_{eff}	14
3.3.3 Affects of V_{dep} due to Annealing via N_{eff} Analysis	16
3.3.4 PIN Diodes	18
4 Probe Station Experimental Setup	20
4.1 Experimental Setup Overview	20

4.2	Electrical Characterization	21
4.2.1	Capacitance-Voltage Measurement (IV)	21
4.2.2	Current-Voltage Measurement (CV)	22
4.3	Environmental Control	22
4.3.1	Temperature Control	22
4.3.2	Dew-Point / Humidity Control	23
4.4	Test Diodes	23
4.4.1	DZero Diodes	23
4.4.2	PIN Diodes	24
4.4.3	2S and PSS Halfmoon Diodes	24
4.4.4	HGCAL Diodes	25
5	Alibava Station Experimental Setup	27
5.1	Test Diodes	27
5.1.1	2S and PSS Halfmoon Diodes	27
5.2	Radioactive Source	27
5.3	Environmental Control	27
5.4	Measuring Halfmoon Diodes	27
5.4.1	Printed Circuit Board	27
6	Irradiating at RINSC	29
6.1	Rabbit	29
6.2	Beam-Port	29
7	Analysis	30
7.1	Hamburg Model Analysis	30
7.1.1	Ljubljana Diodes	30
7.1.2	HGCAL Diodes	34
7.2	PIN Analysis	34
7.2.1	Temperature Study	34
7.2.2	Annealing Study	34
8	Conclusions	39

8.1	Effects of Concurrent Annealing and Irradiation	39
8.2	RINSC-Ljubjana Cross Calibration	39
	Bibliography	42
	Appendix	43

List of Figures

1.1	CERN Complex (from [4])	2
1.2	Integrated particle fluence in 1MeV neutron equivalent per cm^2 for the CMS Phase-2 Tracker (from [17])	3
1.3	CMS Detector Diagram (from [12])	3
2.1	Example of doping in Silicon (from [10])	5
2.2	Pn-junction under electrically neutral conditions (from [2])	6
2.3	Typical IV Curve (from [11])	8
2.4	Typical CV Curve (from [11])	9
3.1	Displacement Damage Functions $D(E)$ (from [9])	13
3.2	Fluence Dependence of Leakage Current for Silicon Detectors (from [9])	15
3.3	Current Related Damage Rate α as a Result of Cumulated Annealing Times at Different Temperatures (from [9])	16
3.4	ΔN_{eff} versus cumulative annealing at 60°C (from [9])	17
3.5	PIN Fluence Studies at Different Pulsed Currents (from [5])	18
4.1	Picture of the set-up we use for electrically characterizing different silicon diodes at Brown University	20
4.2	Diagram of the sensor and chuck setup in the probe station	21
4.3	(a) The full DZero halfmoon before separating the sensors, (b) Picture of the large diode on the DZero cutout, the top needle is grounded and touching the guard ring pad while the lower needle is touching the bias pad	23
4.4	(a) Uncut full halfmoon sensor from Hamamatsu, (b) Electrically characterizing the sensors below the strip sensors, a process which is done pre-irradiation as well as twice post-irradiation	24
4.5	Electrically characterizing HGCAL diodes to be used to determine fluence from irradiation runs conducted in the beamport at RINSC .	25

5.1	Picture of the halfmoon cut out with strip test structures in the Alibava setup and a strontium source hovering over the strips	28
5.2	(a) Previous way of attaching halfmoon connections to Alibava setup, (b) Printed circuit boards to be used to reliably connect to halfmoon components	28
7.1	Ljubljana Hamburg analysis of DZero diodes to determine possible transportation annealing en route to Brown University from Slovenia	30
7.2	Hamburg analysis of HGCAL diodes irradiated at RINSC for 43 minutes. (a) HGCAL diode at back of beamport, (b) HGCAL diode at front of beamport, (c) temperature profile from start of irradiation to them being pulled out.	31
7.3	Hamburg analysis of HGCAL diodes irradiated at RINSC for 86 minutes	31
7.4	Hamburg analysis of HGCAL diodes irradiated at RINSC for 216 minutes	32
7.5	Hamburg analysis of HGCAL diodes irradiated at RINSC for 86 minutes	32
7.6	Hamburg analysis of HGCAL diodes irradiated at RINSC for 118 minutes	33
7.7	Hamburg analysis of HGCAL diodes irradiated at RINSC for 43 minutes	33
7.8	Hamburg analysis of HGCAL diodes irradiated at RINSC for 32 minutes	34
7.9	Calculated the time it took for the PIN diode to reach 95% of its saturation voltage	35
7.10	Result of PIN-thermometer analysis, found that ramp-up-time would significantly affect cumulative annealing time for short-duration annealing	36
7.11	Normalized forward voltage (V_f) vs. cumulative annealing time for PIN-diodes	37
7.12	Exponential scale factor vs. temperature for PIN diodes	38
8.1	Calculated fluence of PIN and D0 diodes vs. Ljubljana anticipated values	39

Chapter 1

Introduction

1.1 The Large Hadron Collider

At the Large Hadron Collider, there are four main experimental setups: CMS, LHCb, Atlas and Alice (as seen in figure 1.1). The Compact Muon Solenoid (CMS) is a multipurpose detector and has been primarily focused on observing new signatures of physics such as the Higgs particle or the lightest supersymmetric particles (SUSY). In order to achieve these objectives, as well as other similar ones, the detector needs to be able to precisely measure the four momenta of the muons, electrons, photons and charged particles over a large energy range [3].

The following chapter will serve as a guide to the LHC in general, with special focus to the coming High-Luminosity LHC upgrade and also to the workings of the CMS detector and it's silicon sensors which serve as the focus of this thesis.

1.1.1 The High-Luminosity Large Hadron Collider (HL-LHC)

The LHC is the world's largest and most powerful particle accelerator [15]. It was built between 1998 and 2008, when it was first started up. The LHC consists of a 27-kilometer ring of super conducting magnets, this ring accelerates the particles to just below the speed of light before they are forced to collide within the designated positions within the detectors. These counter-circulating beams meet with a total collisional energy of 13 TeV at which moment the detectors work to determine the characteristics of the offspring in order to gain insight into the underlying physics which occurred at the moment of collision.

The High-Luminosity LHC (HL-LHC) is a major upgrade of the LHC, the LHC collides tiny particles of matter (protons) in order to study the fundamental com-

CERN's Accelerator Complex

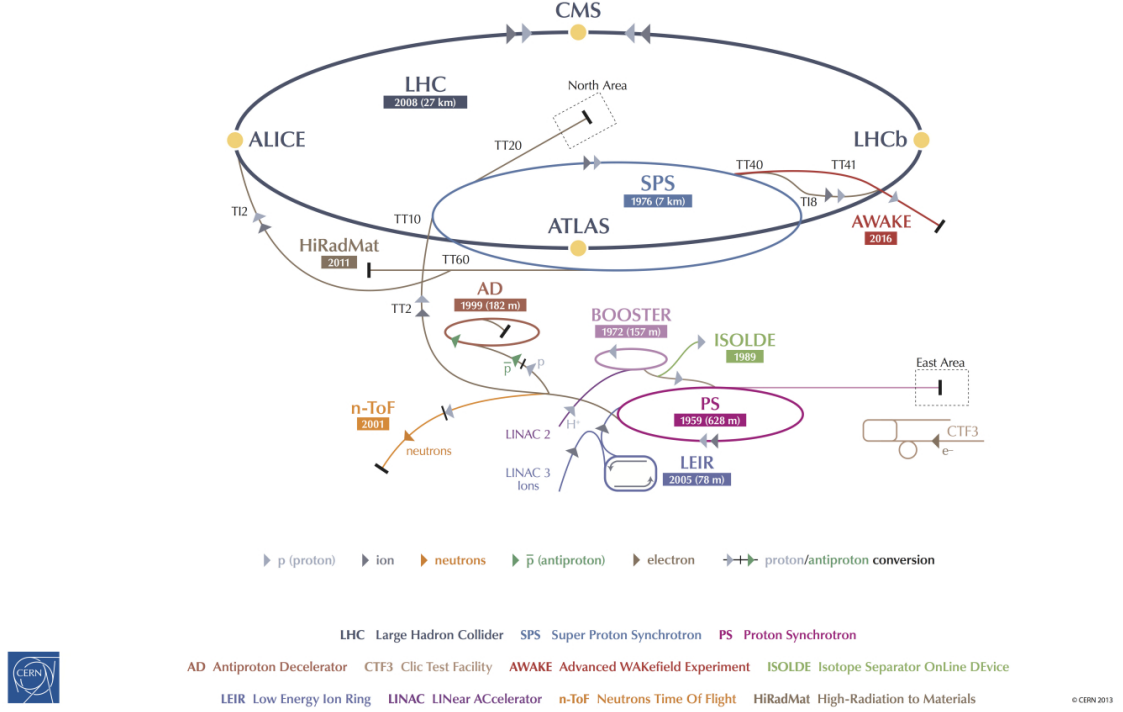


Figure 1.1: CERN Complex (from [4])

ponents of matter and the forces that bind them together, the HL-LHC will allow operators the ability to study these events in more detail by increasing the number of collisions by a factor of 5 – 7 from where they were prior to the upgrade [14]. Luminosity is the measure of the number of potential collisions per surface unit area over a given period of time [14], this quantity integrated is measured in inverse fentobarns [fb^{-1}]; where one inverse fentobarn represents 100 million million collisions.

In figure 1.2 we see the integrated particle fluence in 1 MeV neutron equivalent (n_{eq}) per cm^2 , where the estimates in the figure correspond to the total integrated luminosity of $3000 fb^{-1}$ of pp (proton-proton) collisions at $\sqrt{s} = 14$ TeV [17]. Of course not all sections of the CMS detector will see the same amount of fluence over the period of operation for phase-2, in figure 1.3 we can see the different layers of CMS where each of the different types of sensors operate. If we compare the two figures, we'll notice that it is expected that the pixel detector could receive up to $1.0 \cdot 10^{16} MeV n_{eq} cm^{-2}$ while the strip sensors which are housed further from the

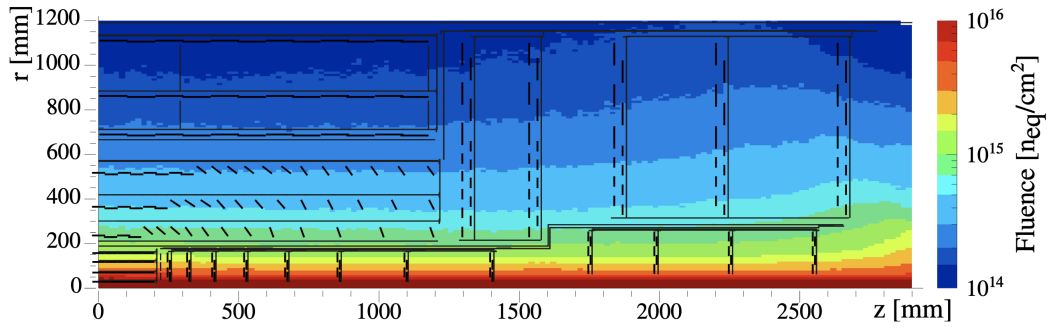


Figure 1.2: Integrated particle fluence in 1MeV neutron equivalent per cm^2 for the CMS Phase-2 Tracker (from [17])

beam path could receive up to $1.0 \cdot 10^{15} \text{ MeV } n_{eq} \text{ cm}^{-2}$ over the course of phase-2 operations. This level of radiation is a concern for any materials, though especially important for the questions of extended accuracy and precision of the silicon particle sensors. It is because of that reasons that there has been extensive research and development of radiation hard materials for the trackers [9].

1.2 The Compact Muon Solenoid Experiment at CERN

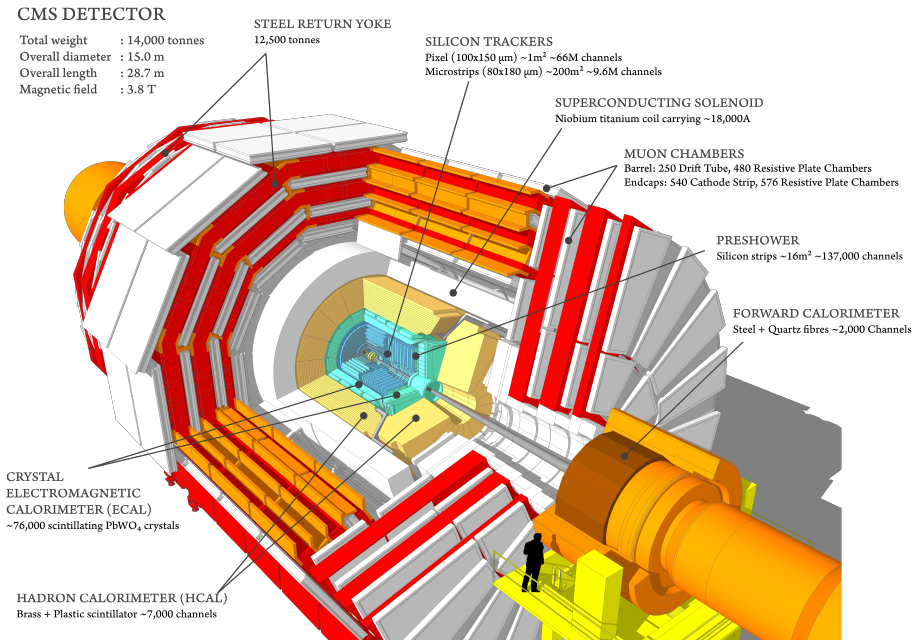


Figure 1.3: CMS Detector Diagram (from [12])

1.2.1 Silicon Sensors

The by-product of the collisions hit the silicon sensors before any of the other detector elements, the reason why they are the first items the particles encounter is because they are used to reconstruct the paths of the particle off-spring with extremely high precision - effectively working as electronic ionization chambers. These paths are then used to determine information about what exactly were the by-products of the collisions. Three designs of silicon sensors are used in the CMS Phase-2 Outer Tracker, all of the types used are n-in-p (highly n-doped strips in p-doped bulk) with p-stop strip isolation [1].

1.2.1.1 Pixel Detectors

The pixel detector contains about 65 million pixels, allowing it to track the paths of particles emerging from the collision with extreme accuracy due to the sensor being able to activate on a very small area as compared to the strip sensor. It is also the closest detector to the beam pipe, with cylindrical layers at 4cm, 7cm and 11cm and disks at either end [13]. Each of the silicon pixel sensors are $100\mu m$ by $150\mu m$, and each of these pixels are connected via bump-wire-bonds to the channels of the readout electronics. The bump-bonds are tiny solder balls have to be put on every cell with relatively high precision [10].

1.2.1.2 Strip Sensors

Directly outside of the region where the silicon pixel detectors are found are the outer tracker modules where two main types are found, the $2S$ and PS modules. The $2S$ modules use two strip sensors with an area of $10^2 cm^2$. Now, the $2S$ sensors are designed with a segmentation along its strips and this results in two rows with 1016 strips with a length of $5cm$ and a pitch of $90\mu m$ [10]. Now, the PS sensors uses a strip ($PS - s$) and a macro-pixel sensor ($PS - p$) with an area of $5 \cdot 10 cm^2$ each.

Chapter 2

Silicon Detectors

The are a number of factors that went into the selection of silicon for the material comprising the particle sensors. Understanding the properties of semiconductor sensors and silicon in general is crucial for the later work that follows, this chapter will sever to briefly summarize some of the main features.

2.1 Silicon Sensor Properties

Silicon has four valence electrons, and when it's in crystalline form all four valence electrons are shared in covalent bonds with neighbouring silicon atoms. In order to make the transportation of electrons easier within the lattice of the silicon it is common practice to change the electrical properties of a semiconductor by adding (doping) different elements into the structure of the silicon crystal lattice. There are two types of dopants, the first type adds one additional electron to the lattice region due to their being five valence electrons on the dopant atom. This type of silicon is labeled n-doped and the concentration of donors is typically N_D , typically phosphorous is used as the donor atom.

The second type adds a positive "hole", the hole is created when the dopant has

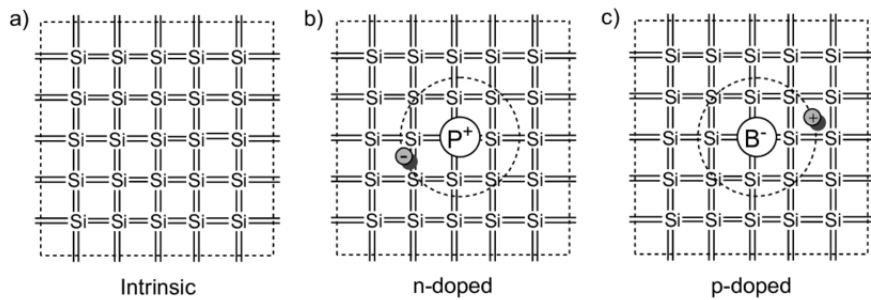


Figure 2.1: Example of doping in Silicon (from [10])

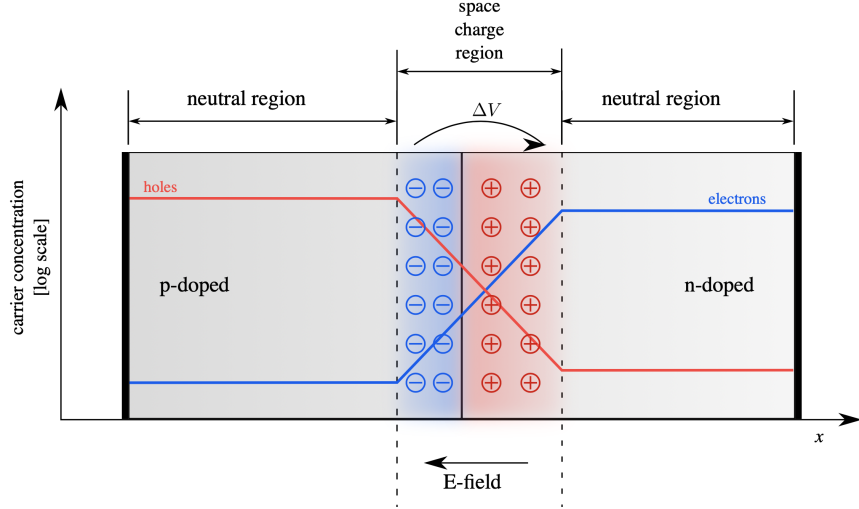


Figure 2.2: Pn-junction under electrically neutral conditions (from [2])

only three valence electrons, and so the region surrounding the dopant is effectively missing one electron. This type of silicon is called p-doped and typically boron or aluminum is used. The concentration of acceptors is labelled N_A .

In figure 2.1 we can see a pictorial representation of the different silicon types (a) shows Intrinsic silicon, (b) shows a n-type Si with donor (phosphorus). Finally in (c) we see a p-type Si with acceptor (boron). Typical values for the doping concentration range between 10^{12} cm^{-3} and 10^{18} cm^{-3} [7].

2.1.1 PN Junction

In figure 2.2 we see the simplest pn-device which is referred to as a pn-junction. The p-doped and n-doped layers of a diode are sandwiched by two parallel metal electrodes. The configuration is comparable to a plate capacitor. Thus, the capacitance of a diode is given by the field constants ϵ , the area of the diode A and the width of the depletion zone w seen in equation 2.1:

$$C = \epsilon_0 \epsilon_{Si} \frac{A}{w} \quad (2.1)$$

A positive terminal connected to the p-doped region and a negative terminal connected to the n-doped region will affect the space charge region of the pn-junction by reducing the electric field and thus reducing the width of the depletion region.

This is known as forward biasing, while connecting the terminals the other way around is simply called reverse biasing.

Applying a bias voltage V in the reverse direction to the sensor, the region of ionized acceptors and donors is named the space-charge-region (which can be seen in figure 2.2) and the effective potential is

$$V + V_{bi} = \frac{1}{e} (E_i^p + E_i^n) = \frac{k_B T}{e} \ln \left(\frac{N_A N_D}{n_i^2} \right) \quad (2.2)$$

Now, the thickness of the space charge region is $W = d_p + d_n$ and can be given as (calculation found in [6])

$$w(V) = \sqrt{\frac{2\epsilon_0\epsilon_{Si}}{e} \left(\frac{1}{N_A} + \frac{1}{N_D} \right) (V + V_{bi})} \quad (2.3)$$

where V_{bi} is the so-called built-in-voltage, N_A is the concentration of acceptor atoms, N_D is likewise the concentration of donor atoms, ϵ_0 is the permittivity of vacuum and ϵ_{Si} is the permittivity of silicon where $\epsilon_{Si}/\epsilon_0 \approx 11.8$. Typically V_{bi} is usually insignificant compared to the bias applied to the sensors so we can approximate the depletion region as

$$w(V) \approx \sqrt{\frac{2V\epsilon_0\epsilon_{Si}}{eN_D}} \quad (2.4)$$

Now, in order to utilize the entire piece of silicon for detecting particles we need to expand this depletion region over throughout the entire thickness of the silicon detector. The voltage at which this is achieved is called the depletion voltage (V_{dep}) and is given by

$$V_{dep} = \frac{eN_D d^2}{2\epsilon_0\epsilon_{Si}} \quad (2.5)$$

In a reverse bias situation the leakage current versus applied voltage follows a characteristic pattern (as seen in figure 2.3). The breakdown is defined as the rapid increase of the current when the reverse bias goes above a certain limit (V_{BD}).

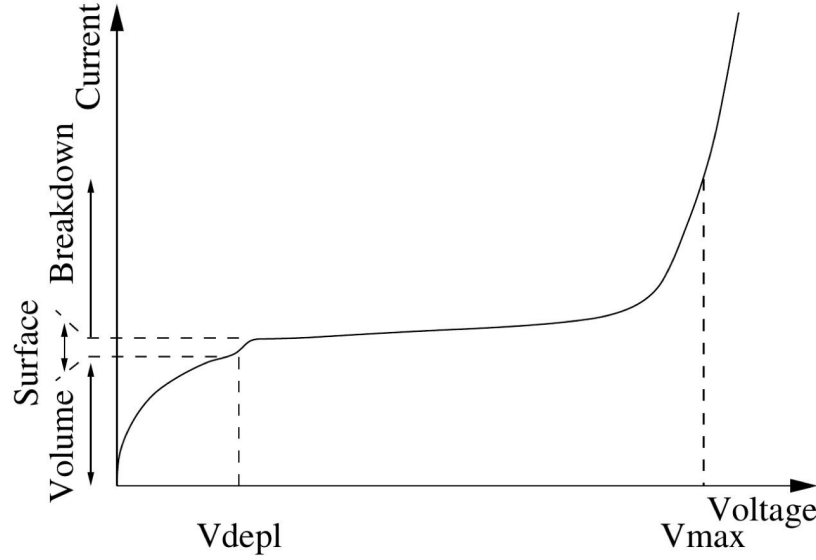


Figure 2.3: Typical IV Curve (from [11])

Now in the case of measuring the capacitance we can refer to the following equation

$$w(V) = \sqrt{\frac{2\epsilon_0\epsilon_{Si}}{e} \left(\frac{1}{N_A} + \frac{1}{N_D} \right) (V + V_{bi})} \quad (2.6)$$

where the built-in voltage V_{bi} can be neglected because $V \gg V_{bi}$ is assumed, which is the case in the operation of silicon detectors. The important thing to note is that the depleted region increases linearly with the square root of the bias

Now one could then use eqn. 2.6 and substitute it into eqn. 2.1 to arrive at the following conclusion

$$C = \epsilon_0\epsilon_{Si}A \frac{eN_A N_D}{\sqrt{2\epsilon_0\epsilon_{Si} (N_A + N_D) (V + V_{bi})}} \quad (2.7)$$

We can see that the capacitance will decrease proportionally with the square root of the bias voltage until the region of depletion extends over the entire volume of the diode, we call this phenomena full depletion and label the voltage at which this occurs V_{dep} . At voltages higher than the depletion voltage we see a constant capacitance where the value of the capacitance for this regime corresponds to the

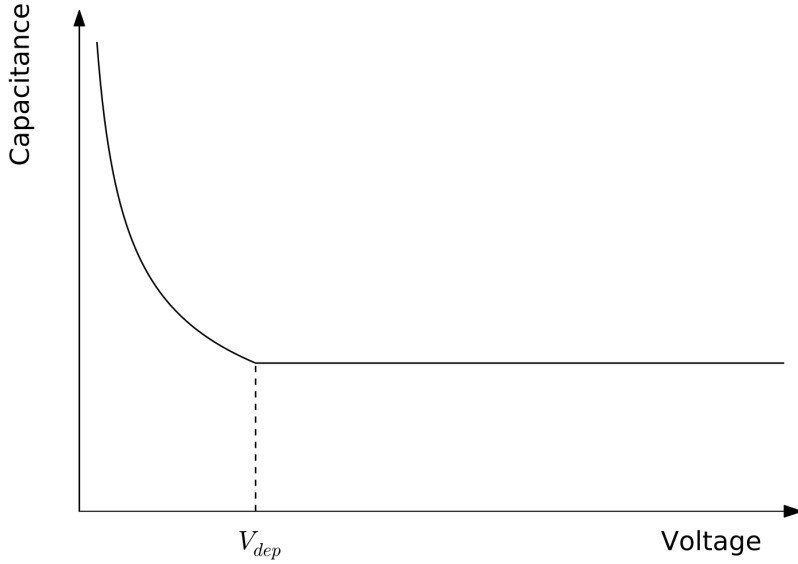


Figure 2.4: Typical CV Curve (from [11])

geometrical capacitance of the diode when considered as a parallel plate capacitor. The value of the capacitance for that situation is:

$$C = \epsilon_0 \epsilon_{Si} \frac{A}{d} \quad (2.8)$$

where d is simply the total thickness of the diode. Additionally, one can express the reverse current dependence on the temperature by

$$I \propto T^2 \cdot e^{-\frac{E_g}{2k_B T}} \quad (2.9)$$

where E_g is the energy gap of the silicon being biased. In our own research we found it very useful to be able to convert between leakage currents at one temperature and leakage currents at another temperature, we did that using the following formula

$$I(T) = I_{tot} \cdot \left(\frac{T}{T_0} \right)^2 \cdot e^{-\frac{E_g}{2k_B} \left(\frac{1}{T_0} - \frac{1}{T} \right)} \quad (2.10)$$

where I_{tot} is the measured leakage current at T_0 , T is the temperature, E_g is the band gap energy of silicon and k_B is of course the Boltzmann constant. Now, as

we will cover in the following chapter, as silicon is damaged by radiation the leakage current per unit volume ΔI increases linearly with fluence Φ_{eq} [9], the slope of this linear relationship is called the current related damage constant (α) and can be seen in the following equation

$$\Delta I = \alpha \Phi_{eq} V \quad (2.11)$$

Chapter 3

Radiation Damage

Generally speaking, in high energy physics (HEP) experiments, the aim of the silicon tracking detectors is the detection of particles passing through the device which makes use of the radiation-matter interactions. Although as one can imagine, the very nature of these interactions can significantly alter the nature of the detector when these kinds of interactions are numerous and over a long period of time. Of course this is of large concern for the HL-LHC upgrade, and so fully characterizing the effects is of great importance. Permanent radiation damage can manifest in two predominate ways, those ways being bulk and surface damage. Though it is the bulk damage which is typically the limiting factor for the use of silicon detectors in HEP experiments, so it is this regime the chapter will primarily focus on. Further reading on both surface and bulk damage can be found in the PhD Thesis by Michael Moll [9].

The following chapter will cover radiation damage mechanisms, characterizations of those changes, and the behavior of those changes with respect to temperature after irradiation.

3.1 Bulk Silicon Damage

Silicon bulk damage is due primarily to impinging particles hitting silicon atoms out of their original place in the crystal lattice. When an incoming particle first hits a silicon atom in the crystal lattice it is called a "primary knock-on atom" (PKA). The PKA then leaves its original lattice site which results in a silicon interstitial and a vacancy where the atom originally was (Frenkel Pair). What Van Lint found was that the primary recoil atom could only be displaced if the energy imparted by the oncoming particle was more than some displacement threshold energy $E_d \approx 25eV$

[16]. One could make a simple non-relativistic calculation for the energy that could be transmitted via elastic scattering; if the mass of the incident particle is $m_{incident}$ with kinetic energy $E_{incident}$ then the maximum energy that could be imparted into the silicon atom in the lattice is

$$E_R = 4 \cdot E_{incident} \cdot \frac{m_{incident} \cdot m_{Si}}{(m_{incident} + m_{Si})^2} \quad (3.1)$$

From the above equation and the displacement threshold energy one could calculate the necessary kinetic energy of the incident particle necessary to displace a silicon atom from the lattice, though this is not something I will do here. Refer to [16] and [9] for more information on the subject.

3.2 Non-Ionizing-Energy-Loss (NEIL) Hypothesis

When considering the particles incident on the silicon detectors, its not the charged hadrons we need to worry about too much - this is because they interact primarily by the coulomb interaction and so most of these interactions only lead to ionization. What needs to be considered however are the neutrally charged neutrons which only interact with the nucleus of the silicon atoms. Most of the interactions between neutrons and the silicon nuclei can be modeled as elastic collisions, though at energies above 1.8MeV nuclear reactions can also take place [16].

Now that we know who our likely bulk damaging culprits are (high energy neutrons), we need a way to model how radiation damage scales with particle energy. The model which we use is called the Non-Ionizing-Energy-Loss-Hypothesis, or NEIL hypothesis. The simplifying assumption of the NEIL hypothesis is that the change in the material due to displacement damage scales linearly with the energy of the incident particles, this doesn't account for any spatial considerations of the incident particles or damage due to PKA cascades. In order to arrive at a calculation for the NEIL, one can use the Lindhard-Partition-Function $P(E_R)$ [6] and then the NEIL can be expressed by the displacement-damage-cross-section

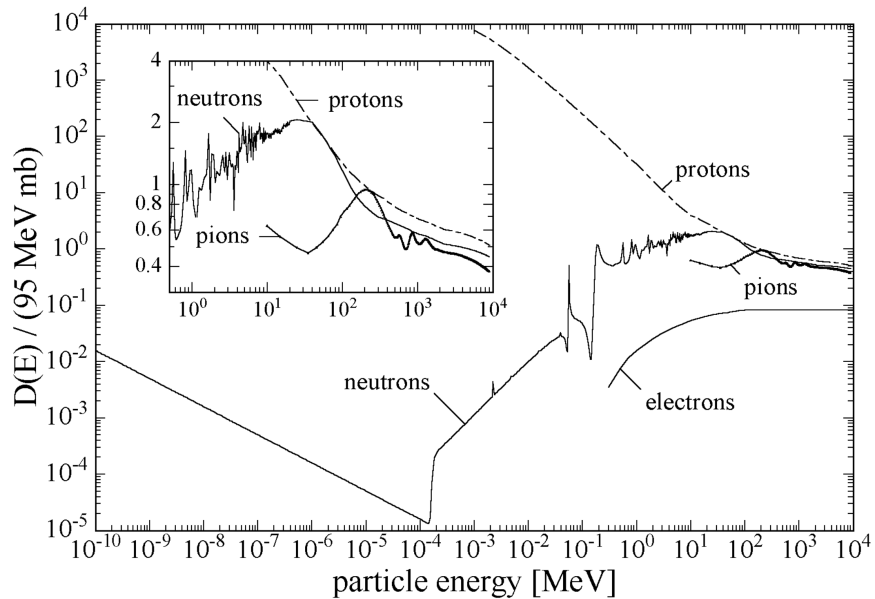


Figure 3.1: Displacement Damage Functions $D(E)$ (from [9])

$$D(E) := \sum_{\nu} \sigma_{\nu}(E) \cdot \int_0^{E_R} f_{\nu}(E, E_R) P(E_R) dE_R \quad (3.2)$$

where ν indicates all possible interactions between the incident particle of energy E and the silicon atoms in the crystal leading to displacement in the lattice. σ_{ν} is the cross section corresponding to the reaction, $f_{\nu}(E, E_R)$ is the probability density function for the generation of a PKA with recoil energy E_R by a particle with energy E . This is then integrated over all recoil energies, where a recoil energy less than the threshold displacement energy ($P(E_R < E_d) = 0$) are identically zero [9]. From this function one can relate experimental fluence and equivalent fluence to one another using a linear relationship: $\Phi_{eq} = \kappa \Phi_{exp}$. The constant κ is called the "hardness factor", and is defined to be identically one for 1 MeV neutrons. The purpose of this is that different experimenters will still be able to compare data taken from samples irradiated by particles at different energies.

3.3 Characterizing Fluence (Φ_{eq})

When developing radiation hard silicon detectors it is important to evaluate the amount of radiation damage that has taken place and how those effects might be reversed. The following sections will serve to illustrate the different approaches we have made in determining the amount of fluence the irradiated silicon sensors have experienced and also how we characterized the temperature affects to the radiation damage. The two main ways we use to characterize the fluence were changes in the leakage current (which scales linearly with the fluence) and the changes to the depletion voltage (which also scaled with the fluence).

3.3.1 Leakage Current

Leakage current is any current which is flowing through the device in question, where it should not be flowing. When the sensor is not irradiated, the leakage current is due primarily to two different processes. The first process being the charge carriers within the doped silicon crossing the junction which is called "diffusion current", and the second cause from the generation of charge carriers in the depletion zone, called "generation current". Experimentally it has been shown that leakage current scales linearly with fluence according to equation 3.3.

$$\alpha\Phi_{eq} = \frac{\Delta I}{V} \quad (3.3)$$

Where in our fluence analysis we are using a value of $\alpha = (3.99 \pm 0.03) \cdot 10^{-17} A/cm$ which we used from the work of R. Wunstorf [18] which was later confirmed by M. Moll [8] to work well for annealing values of 80 min at 60C. In figure 3.2 we can see how well this linear relationship holds for a wide range of parameters.

3.3.2 Effective Doping Concentration N_{eff}

The effective doping concentration is simply the difference between the concentrations of the ionized donors and acceptors within the depletion zone. If one wanted

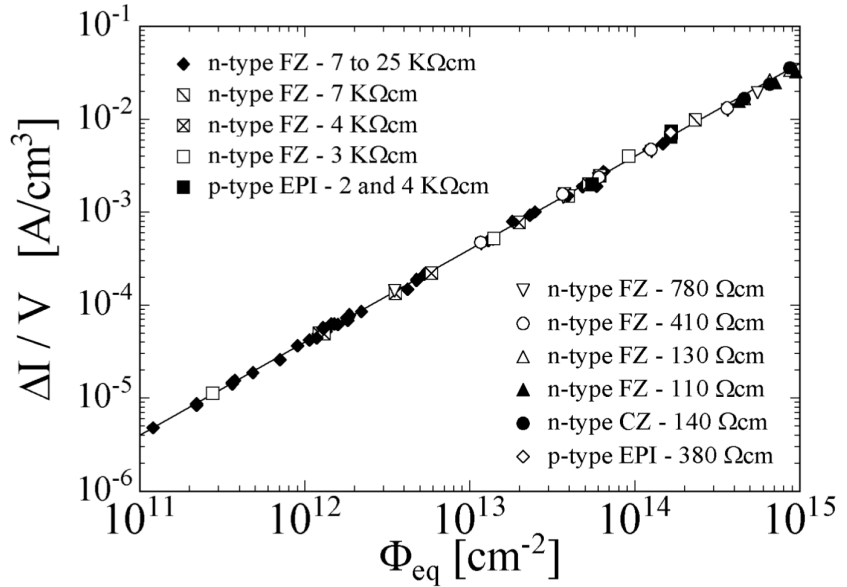


Figure 3.2: Fluence Dependence of Leakage Current for Silicon Detectors (from [9])

to, one could derive the width of the depletion zone as a function of applied voltage and N_{eff} using Poissons equation, something which will not be presented here. That solution is equation 2.6, although written in only a slightly different way below in equation 3.4

$$w(V) = \sqrt{\frac{2\epsilon_0\epsilon_{Si}}{e|N_{eff}|}(V + V_{bi})} \quad (3.4)$$

Now, as we mentioned in the previous chapter we expect that $V \gg V_{bi}$, if we then also have $V = V_{dep}$ we will arrive at the following equation

$$|N_{eff}| = \frac{2\epsilon_0\epsilon_{Si}}{ed^2}|V_{dep}| \quad (3.5)$$

where d is the width of the diode in question. The following section will aim the answer how N_{eff} and V_{dep} are affected by temperature, and what we will find is that there is a combination of temperature and time which will reverse some of the detrimental affects due to radiation damage.

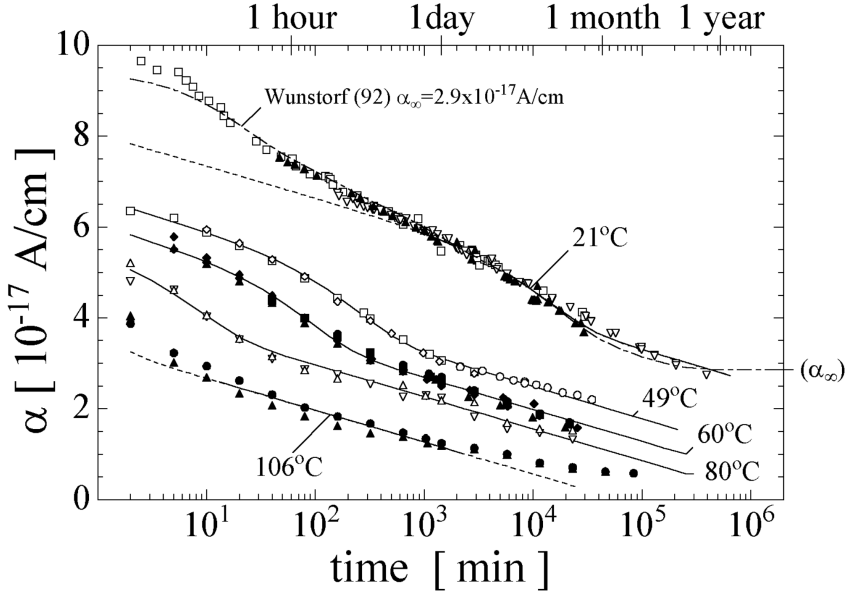


Figure 3.3: Current Related Damage Rate α as a Result of Cumulated Annealing Times at Different Temperatures (from [9])

3.3.3 Affects of V_{dep} due to Annealing via N_{eff} Analysis

V_{dep} shows a very different response to annealing than the leakage current, and that difference can be seen in the change to N_{eff} which is after all proportional to V_{dep} . The change in N_{eff} is described by the Hamburg Model and was given the following parameterization due to M. Moll [9] in his 1999 thesis.

$$\Delta N_{eff}(\Phi_{eq}, t) = N_C(\Phi_{eq}) + N_A(\Phi_{eq}, t) + N_Y(\Phi_{eq}, t) \quad (3.6)$$

where the term $N_C(\Phi_{eq})$ is called the stable damage and is given by the equation below

$$N_C(\Phi_{eq}) = r_C N_{eff,0} \left(1 - e^{-C\Phi_{eq}} \right) + g_c \Phi_{eq} \quad (3.7)$$

more information about each of the terms can be found in the 2006 dissertation by Fugeri [3], and we eventually want to get to a fully described equation for $\Delta N_{eff}(\Phi_{eq}, t)$ which will be used for determining differences in our irradiation pro-

cedures for the HL-LHC silicon sensor test structures. The other terms in equation 3.6 I will list quickly.

$$N_A(\Phi_{eq}, t) = \Phi_{eq} \sum_i g_{a,i} e^{\frac{t}{\tau_{a,i}}} \quad (3.8)$$

Equation 3.8 is for $N_A(\Phi_{eq}, t)$ and is called the beneficial annealing which is the sum of exponential decays of radiation induced damage. Typically these exponential decays can be summarized into one exponential damage decay with a time constant τ_a using a Arrhenius relation, this is the assumption we will make. The last term in 3.6 to speak about is $N_Y(\Phi_{eq}, t)$ which is called the reverse annealing term.

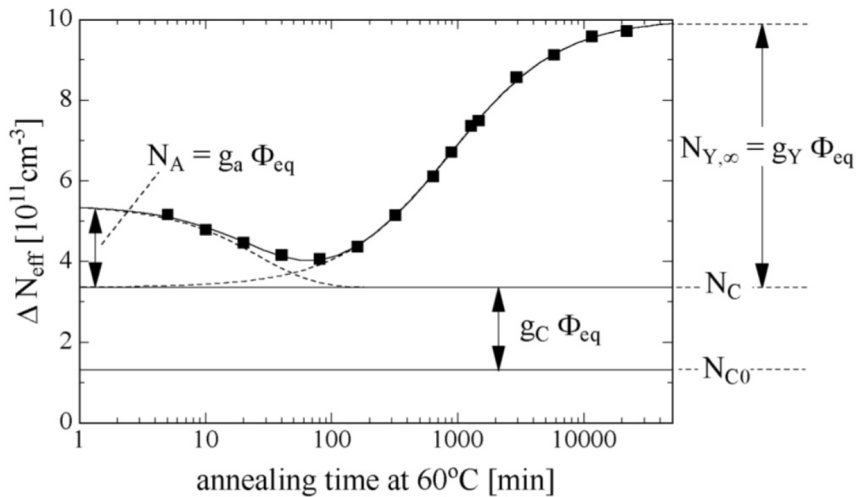


Figure 3.4: ΔN_{eff} versus cumulative annealing at $60^\circ C$ (from [9])

$$N_Y(\Phi_{eq}, t) = g_Y \Phi_{eq} \left(1 - \frac{1}{1 + \frac{t}{\tau_y}} \right) \quad (3.9)$$

Where in equation 3.9 $g_Y = (5.16 \pm 0.09) \cdot 10^{-2} \text{cm}^{-1}$ and the time constant τ_y can be expressed using an Arrhenius plot as was done for the beneficial annealing time constant term from equation 3.8.

$$\Delta N_{eff}(t) = g_a e^{-\frac{t}{\tau_a}} \Phi_{eq} + g_y \left(1 - \frac{1}{1 + \frac{t}{\tau_y}} \right) \Phi_{eq} + r_C N_{eff,0} \left(1 - e^{-C \Phi_{eq}} \right) + g_c \Phi_{eq} \quad (3.10)$$

where $\Delta N_{eff}(t) = N_{eff}(t_{ann}) - N_{eff,pre-irr}$ and g_a is called the beneficial annealing introduction rate, g_y is the reverse annealing introduction rate, τ_a is the beneficial annealing time constant, τ_y is the reverse annealing time constant and Φ_{eq} is of course the equivalent fluence.

Further reading of anticipated parameter values and their significance can be found in [9] and [3]. A typical graph for the effective doping concentration can be seen in figure 3.4, we notice that there is a minimum in ΔN_{eff}

3.3.4 PIN Diodes

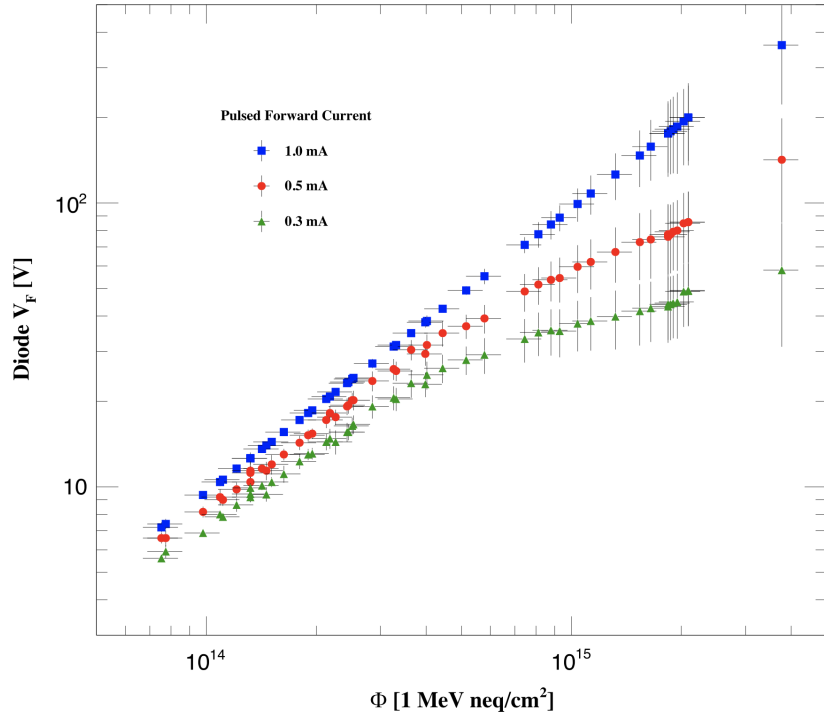


Figure 3.5: PIN Fluence Studies at Different Pulsed Currents (from [5])

In Figure 3.5 from the paper by Hoeferkamp et al. [5], we see diode forward voltage as a function of applied fluence, for three choices of applied current amplitude. The vertical error bars indicate the combined uncertainties related to temperature variation during the irradiation process, current pulse width, and sourcemeter precision. The horizontal error bars indicate the uncertainty deriving from counting statistics on calibration foils in the gamma spectrometer.

Based on the linear fit of Figure 3.5, Hoeferkamp et al. showed a good relation between diode forward voltage and fluence, where the forward voltage was measured after applying a $1mA$ for approximately .38s. That relation is seen in Equation 3.11.

$$\Phi_{neq} = 1.1 \cdot 10^{13} \cdot V_f - 6.2 \cdot 10^{10} \quad (3.11)$$

Chapter 4

Probe Station Experimental Setup



Figure 4.1: Picture of the set-up we use for electrically characterizing different silicon diodes at Brown University

All of the test structures which we electrically characterized were done so on the probe station (pictured in figure 4.1). We call it the probe station because we are able "probe" a sensor using needles (example seen in figure 4.3) on a precise spot, these needles are then connected to different instruments depending on what we're interested in measuring.

4.1 Experimental Setup Overview

We measured n and p-type sensors, irradiated and non-irradiated sensors and at a range of temperatures from $+20^{\circ}C$ to $-20^{\circ}C$. The specific names of the sensors include DZero diodes, 2S and PSS halfmoon diodes, HGCAL diodes and also PIN diodes. For all but the PIN diodes, the sensors were placed in a climate controlled box on an aluminum chuck. The sensor is made to "stick" to the chuck using a

vacuum pump pulling air from small holes on the chuck. If the temperature we are aiming to measure the sensor is below the dewpoint in the box, we can flush the box with nitrogen from an adjacent nitrogen bottle - otherwise we pass air into the box through desiccants to ensure the box is dry.

4.2 Electrical Characterization

The diodes are biased by applying voltage to the entire aluminum chuck by using a Keithley 237 High Voltage Measurement Unit ($\pm 1100V$). This same instrument is then used to measure the current in the bias ring using the probe needle which has a tip width of about $7\mu m$. For diodes which have a guard ring a needle is placed on the pad to ground in order to reduce fringe fields near the bulk material. The guard ring current is measured using a Keithley 6485 Picoammeter.

All of the instruments are controlled by LabView via GPIB, where we can specify parameters like voltage step size, number of measurements taken, whether it is a negative or positive bias and also maximum voltage. Typically, but not always, at each voltage step the measurement is made four independent times half a second apart and an average of those four measurements is quoted.

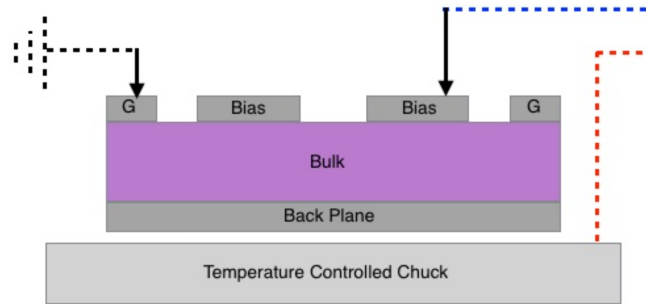


Figure 4.2: Diagram of the sensor and chuck setup in the probe station

4.2.1 Capacitance-Voltage Measurement (IV)

When doing a CV measurement we first ground guard ring and then pass the red and blue lines of figure 4.2 through an isolation box and then to a HP 4284A LCR

Meter which takes the CV measurement. The isolation box helps ensure that the LCR meter doesn't receive voltages which might fry it. Once the signal is received by the LCR meter, the LCR meter will output an AC voltage signal into the circuit at typically two different frequencies ($1KHz$ and $10KHz$) where then the LCR will measure the response to determine the capacitance of the diode.

4.2.2 Current-Voltage Measurement (CV)

When taking an IV measurement, as described briefly above in section 4.2, one needle is placed on the guard ring and another is placed on the bias ring pad (diagram of this situation is seen in figure 4.2). The red line is connected to the Keithley

4.3 Environmental Control

In order to make the measurements made consistent, the probe station has environmental controls which allow for the fine-tuning of a number of parameters relevant to the measurement taking process.

4.3.1 Temperature Control

The current of the diodes being measured is highly temperature dependent, for that reason we require that once a temperature has been set that there be no more than a $\pm 0.05^{\circ}C$ deviation from that temperature. To achieve this result two methods are used, the first is a Julabo FP89-HL Ultra-Low Refrigerated Circulator flows coolant just below the chuck to within a degree or two of the set temperature. The second method employed is a peltier thermoelectric cooler, which cools by using the Peltier effect to create a heat flux at the junction of two different types of materials. This second method then allows for the fine temperature control, where the voltage of the peliter is controlled using a proportional-integral-derivative (PID) controller. All diode measurements made on the probe station kept temperature variations well within $\pm 0.05^{\circ}C$.

4.3.2 Dew-Point / Humidity Control

One of the more crucial aspects to measuring silicon diodes at low temperatures is ensuring no condensation accumulates on surface of the diodes when measuring them. To ensure a dry measuring environment we pass compressed air through desiccant, and if this is not dry enough we use a N_2 bottle during measuring. We monitor the dewpoint in real time via an instrument inside of the measurement box, and generally try and make sure that the dew point is at least $1.5^\circ C$ below the temperature we are measuring at.

4.4 Test Diodes

Below I will describe the diodes measured on the probe station. Unirradiated diodes were measured at $+20^\circ C$, irradiated but pre-annealed diodes were measured at $0^\circ C$ and irradiated and annealed diodes measured at $-20^\circ C$.

4.4.1 DZero Diodes

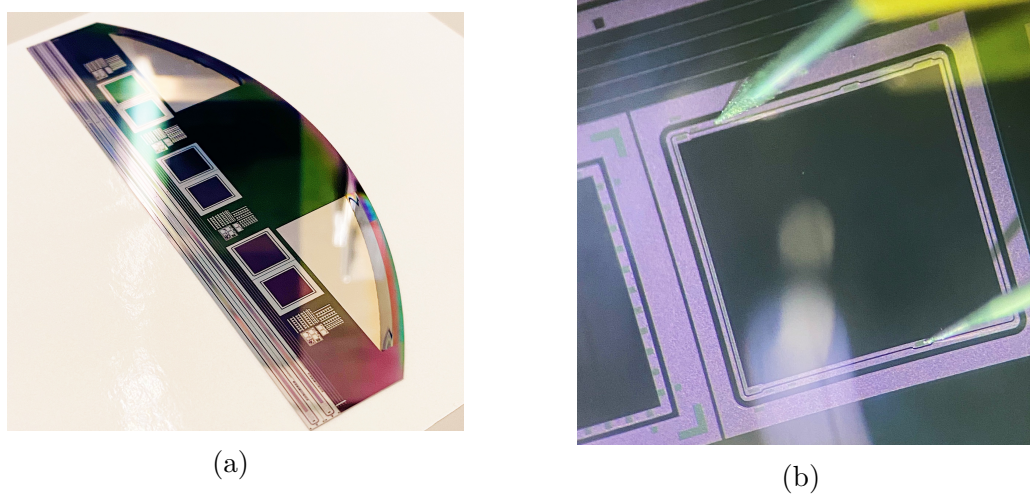


Figure 4.3: (a) The full DZero halfmoon before separating the sensors, (b) Picture of the large diode on the DZero cutout, the top needle is grounded and touching the guard ring pad while the lower needle is touching the bias pad

The predominately measured diode at the probe station is the D0 diodes from an old FermiLab experiment. A picture of the halfmoon we break the diodes away from is shown in figure 4.3 (a), in (b) is a picture of the large diode on the probe

station chuck with one needle on the bias pad and the other needle on the guard ring pad. There are in-fact two diodes on each DZero cutout, though we only utilize the larger of the two because it is the only one with a guard ring surrounding the diodes bulk material. We use these diodes in beamport runs (to be described in section 6.2) and in the rabbit irradiation's (to be described in section 6.1).

4.4.2 PIN Diodes

A PIN diode is a diode with a small, undoped intrinsic semiconductor region between a p-type semiconductor and an n-type semiconductor region. Their accuracy with fluence measurements is limited, so we use them primarily in rabbit fluence runs to estimate longitudinal and face-to-face fluence values. The method by which we measure fluence is described in section 3.3.4

4.4.3 2S and PSS Halfmoon Diodes

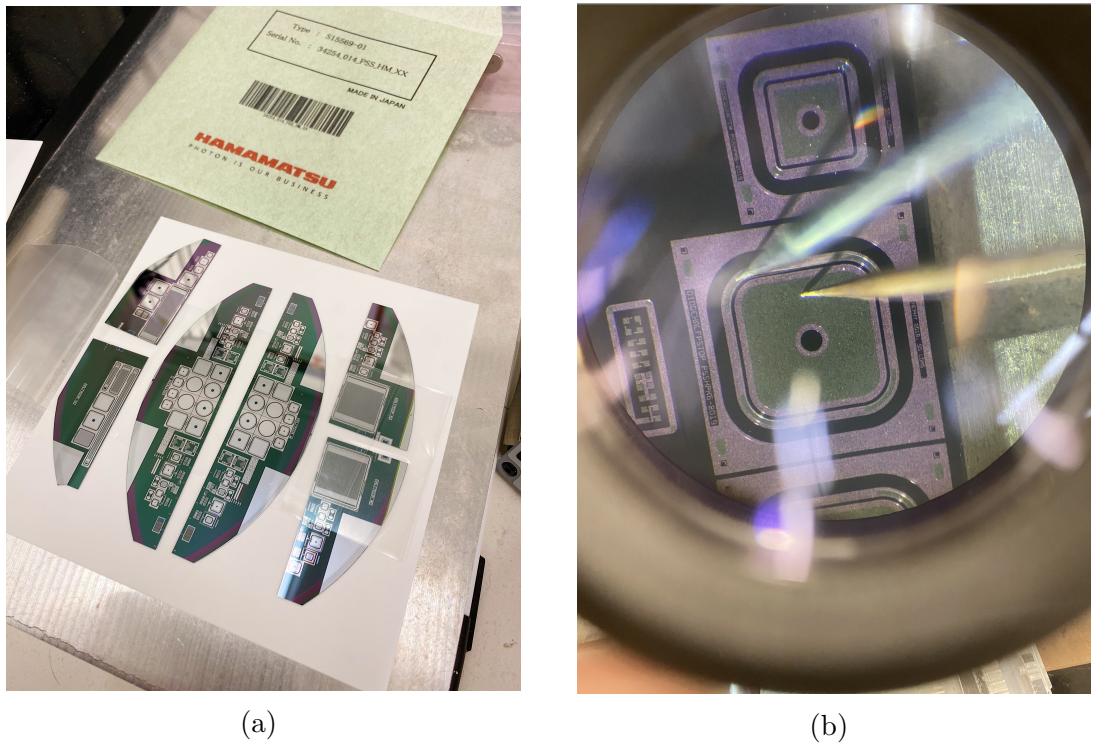


Figure 4.4: (a) Uncut full halfmoon sensor from Hamamatsu, (b) Electrically characterizing the sensors below the strip sensors, a process which is done pre-irradiation as well as twice post-irradiation

The 2S and PSS halfmoon diodes (seen in figure 4.4) we measure on the probe

station are small test structures from the same silicon wafers used for the full-scale sensors to be used at CMS. The irradiation studies we perform on them are analyzed on both the probe and Alibava stations. The probe station we use for electrically characterizing diodes like those seen in figure 4.4 (b), while at the Alibava station we are testing the miniature strip sensors directly below the diodes. That station uses a radioactive source (strontium) to see how well the strips detect after irradiating at different fluences. Further information about that process will be described in chapter 5.

4.4.4 HGCAL Diodes

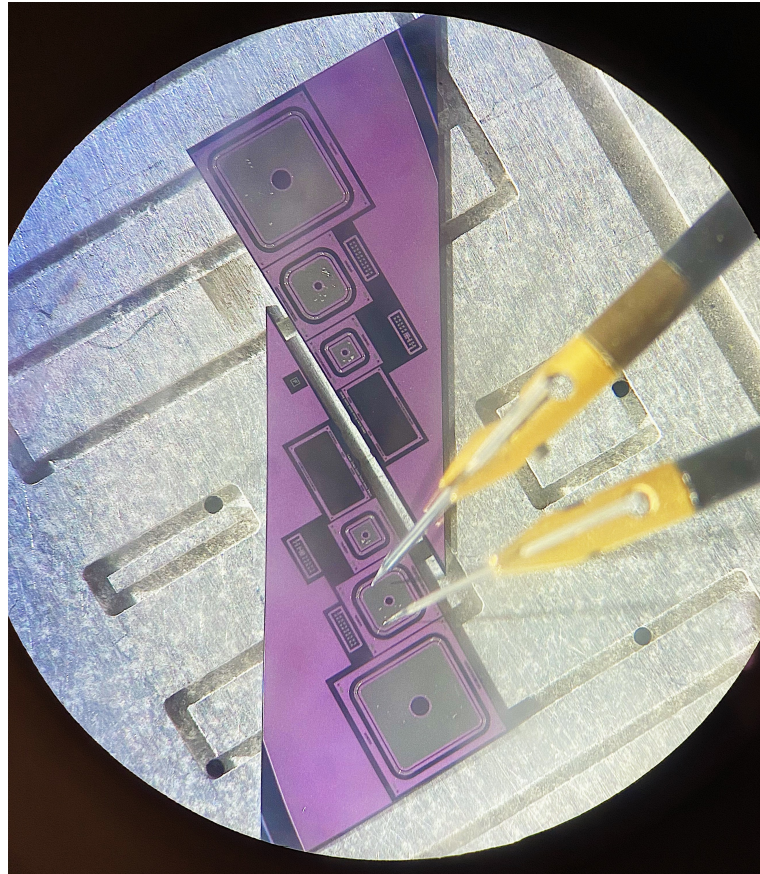


Figure 4.5: Electrically characterizing HGCAL diodes to be used to determine fluence from irradiation runs conducted in the beamport at RINSC

The final test structures to speak about are the HGCAL diodes, these we recently started measuring (only at the end of 2021) and we're measuring them so we can more directly compare the fluence measurements of the other HGCAL members.

One big advantage of the HGCAL diodes is that they have a thinner bulk which allows us to still see a depletion voltage at higher fluences. The other advantage is they have a larger bias pad (being almost the entire area of the diode) and much larger guard ring pads.

Chapter 5

Alibava Station Experimental Setup

5.1 Test Diodes

5.1.1 2S and PSS Halfmoon Diodes

5.2 Radioactive Source

5.3 Environmental Control

The exact same kinds of considerations with respect to temperature control are taken at the Alibava station as they were at the probe station. Differences are only in the rate at which temperature measurements are made and altered. Refer to section 4.3 for more information.

5.4 Measuring Halfmoon Diodes

5.4.1 Printed Circuit Board

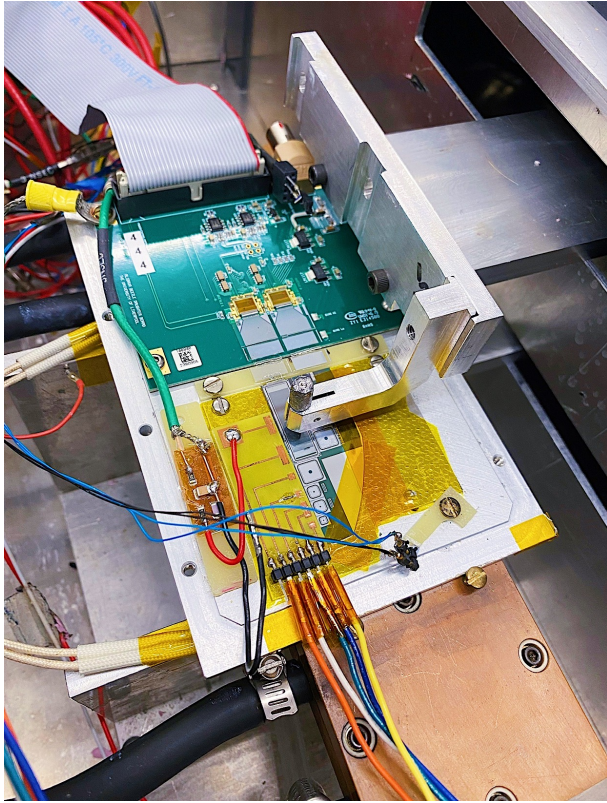


Figure 5.1: Picture of the halfmoon cut out with strip test structures in the Alibava setup and a strontium source hovering over the strips

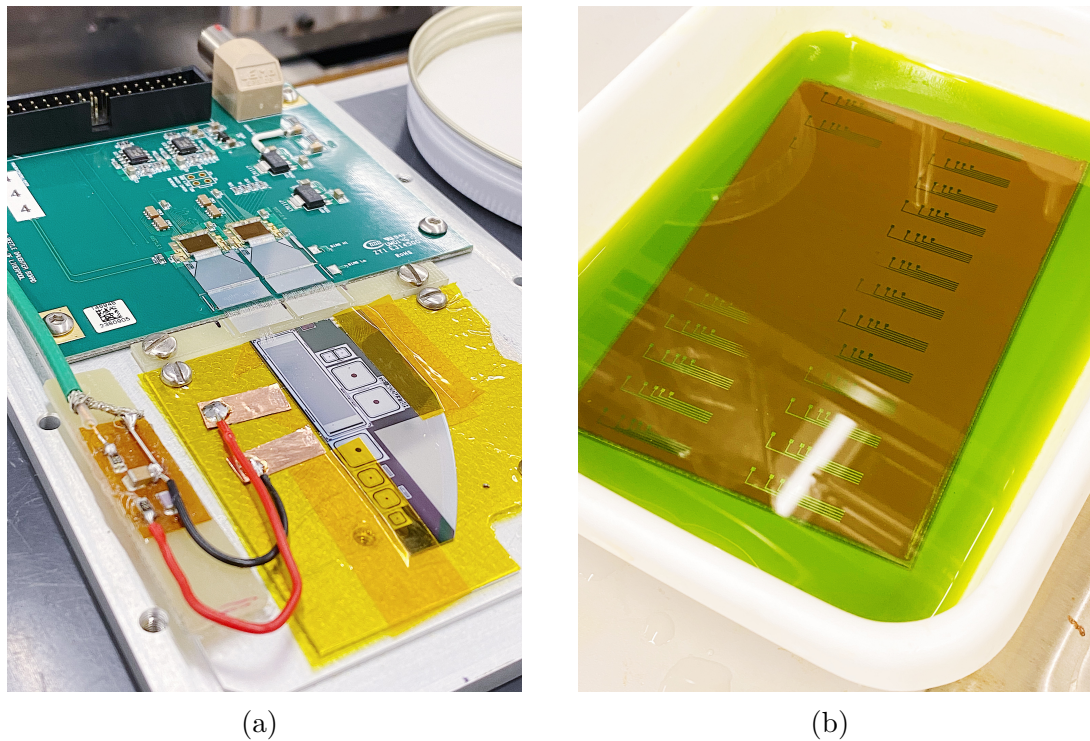


Figure 5.2: (a) Previous way of attaching halfmoon connections to Alibava setup, (b) Printed circuit boards to be used to reliably connect to halfmoon components

Chapter 6

Irradiating at RINSC

6.1 Rabbit

6.2 Beam-Port

Chapter 7

Analysis

7.1 Hamburg Model Analysis

7.1.1 Ljubljana Diodes

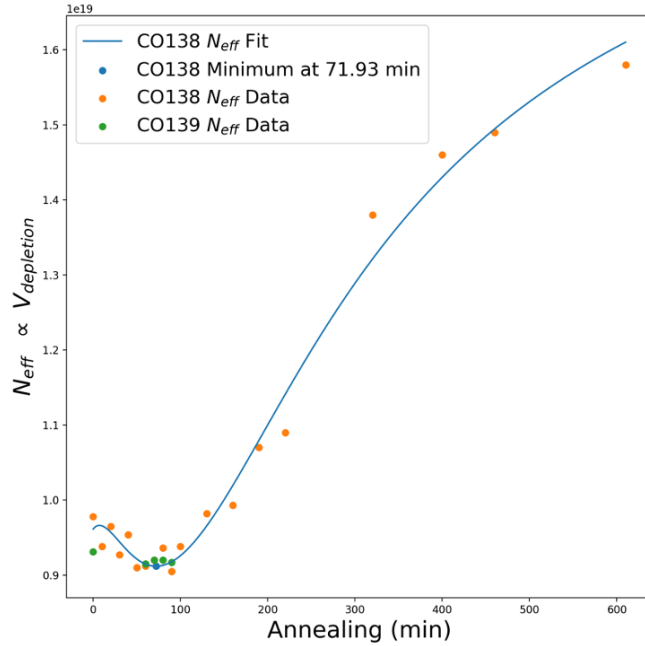


Figure 7.1: Ljubljana Hamburg analysis of DZero diodes to determine possible transportation annealing en route to Brown University from Slovenia

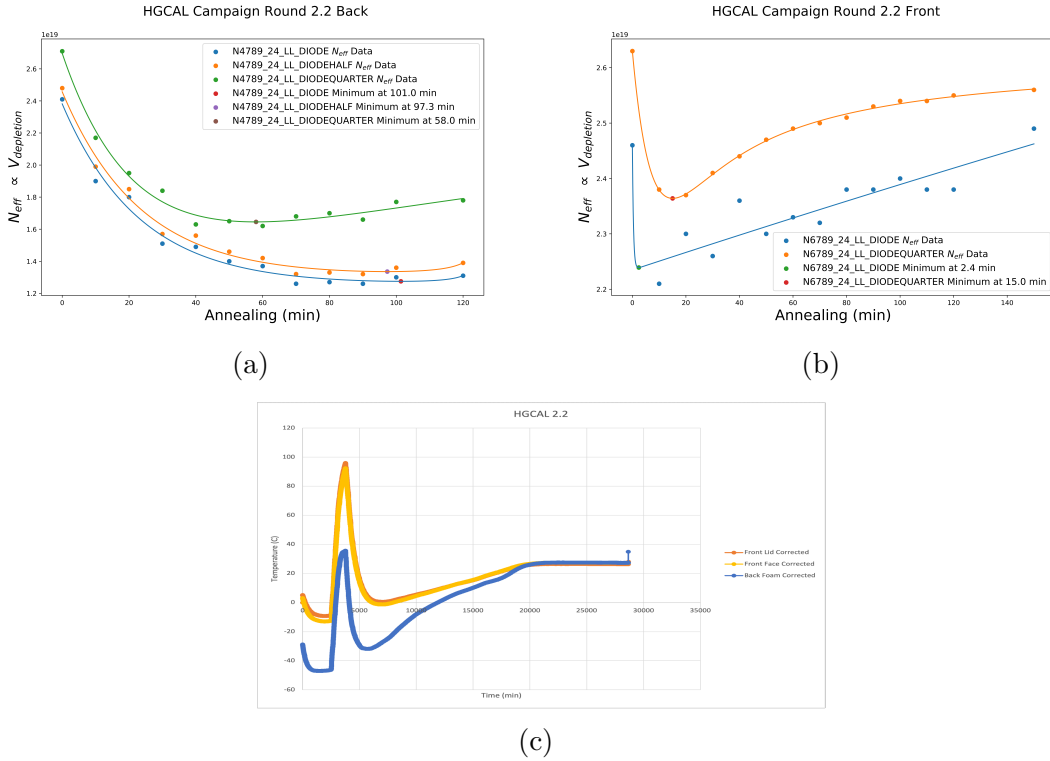


Figure 7.2: Hamburg analysis of HGCAL diodes irradiated at RINSC for 43 minutes. (a) HGCAL diode at back of beamport, (b) HGCAL diode at front of beamport, (c) temperature profile from start of irradiation to them being pulled out.

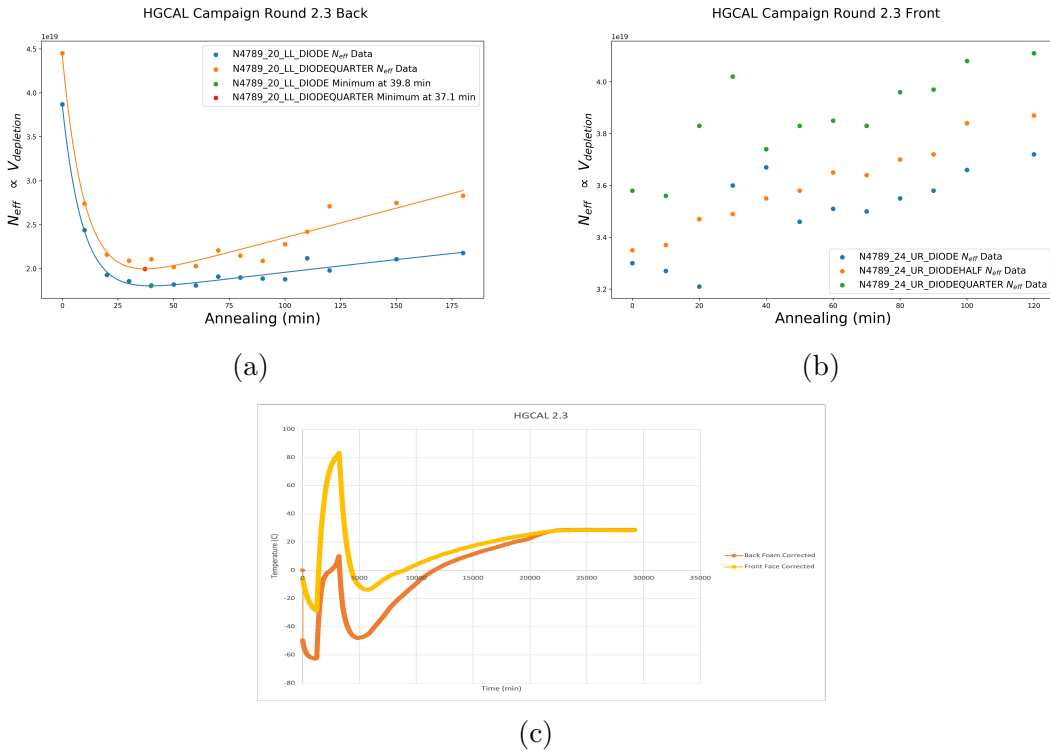


Figure 7.3: Hamburg analysis of HGCAL diodes irradiated at RINSC for 86 minutes

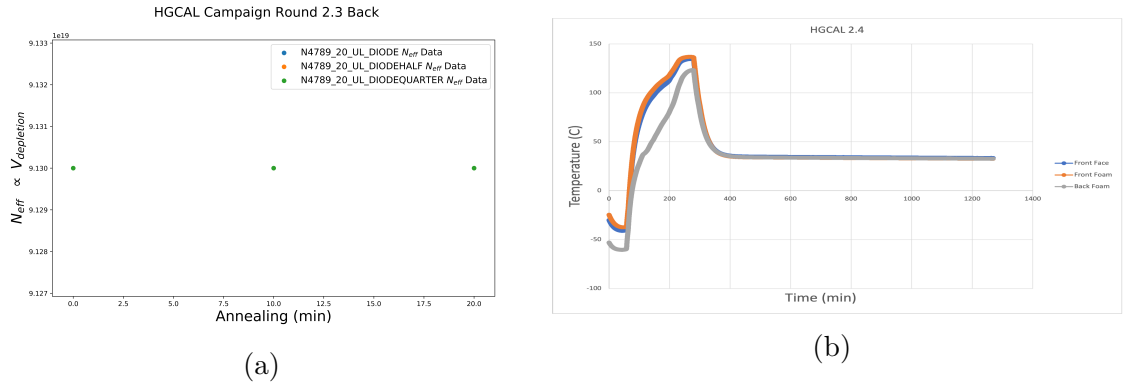


Figure 7.4: Hamburg analysis of HGCAL diodes irradiated at RINSC for 216 minutes

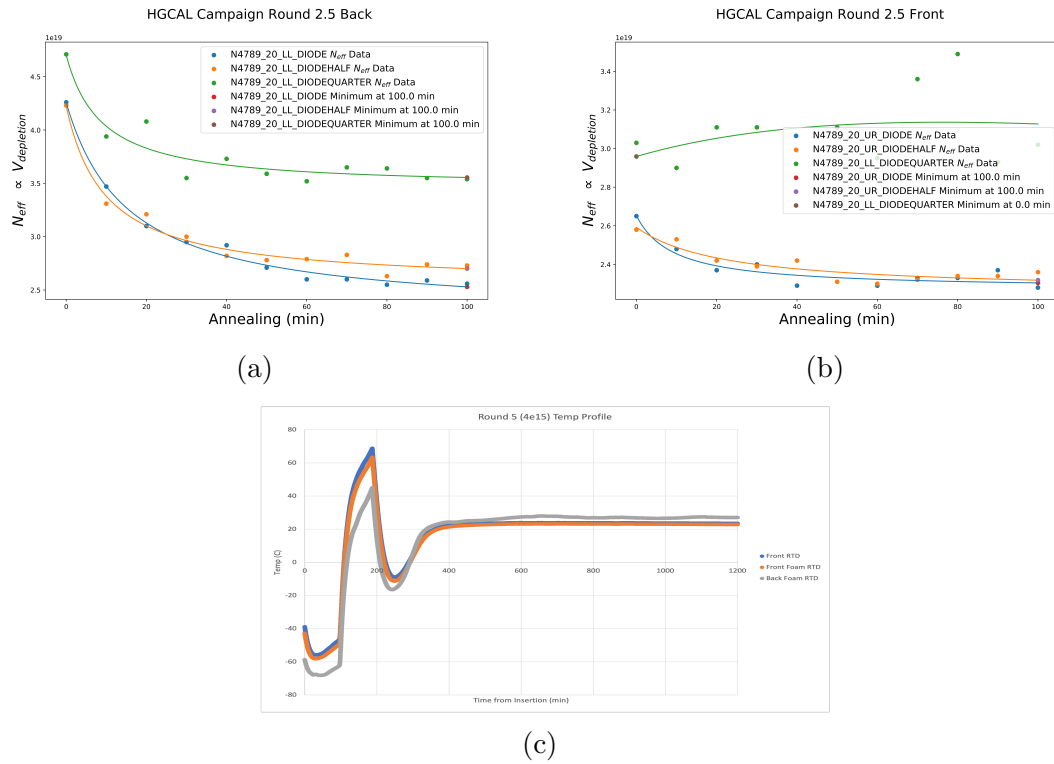


Figure 7.5: Hamburg analysis of HGCAL diodes irradiated at RINSC for 86 minutes

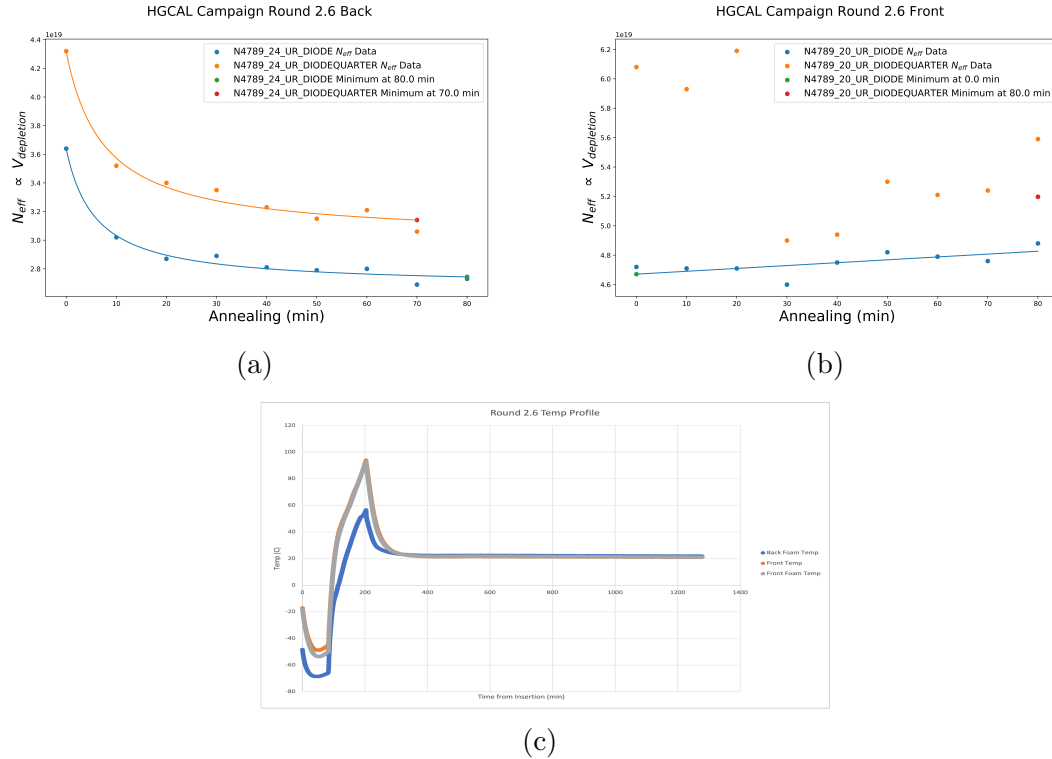


Figure 7.6: Hamburg analysis of HGCAL diodes irradiated at RINSC for 118 minutes

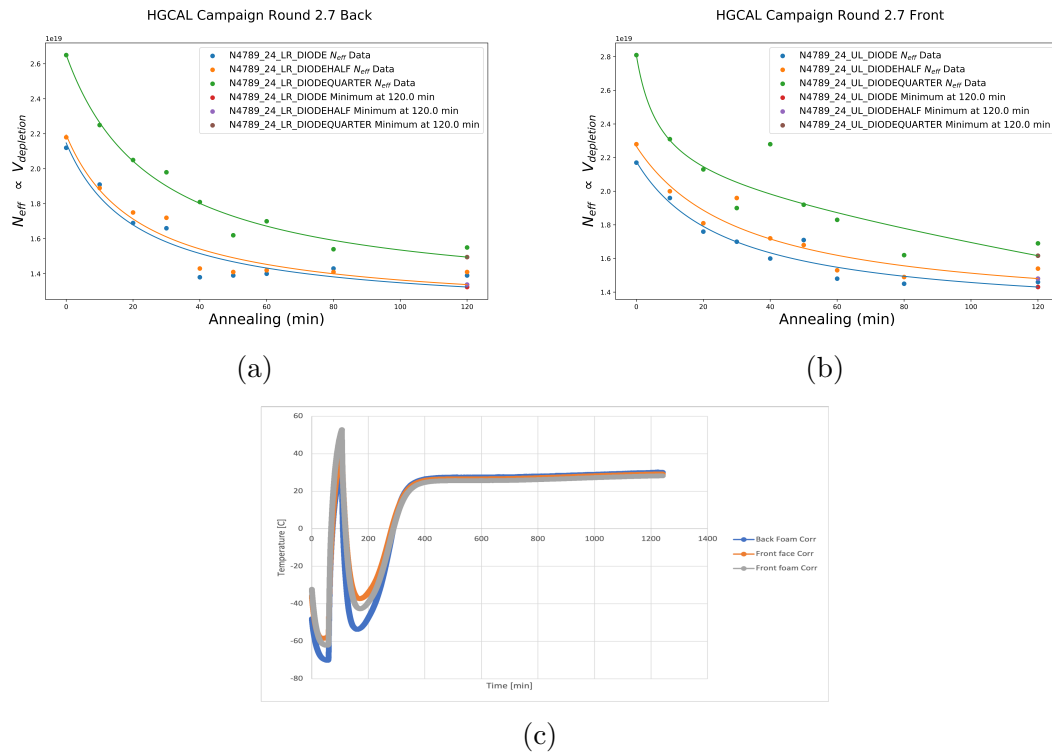


Figure 7.7: Hamburg analysis of HGCAL diodes irradiated at RINSC for 43 minutes

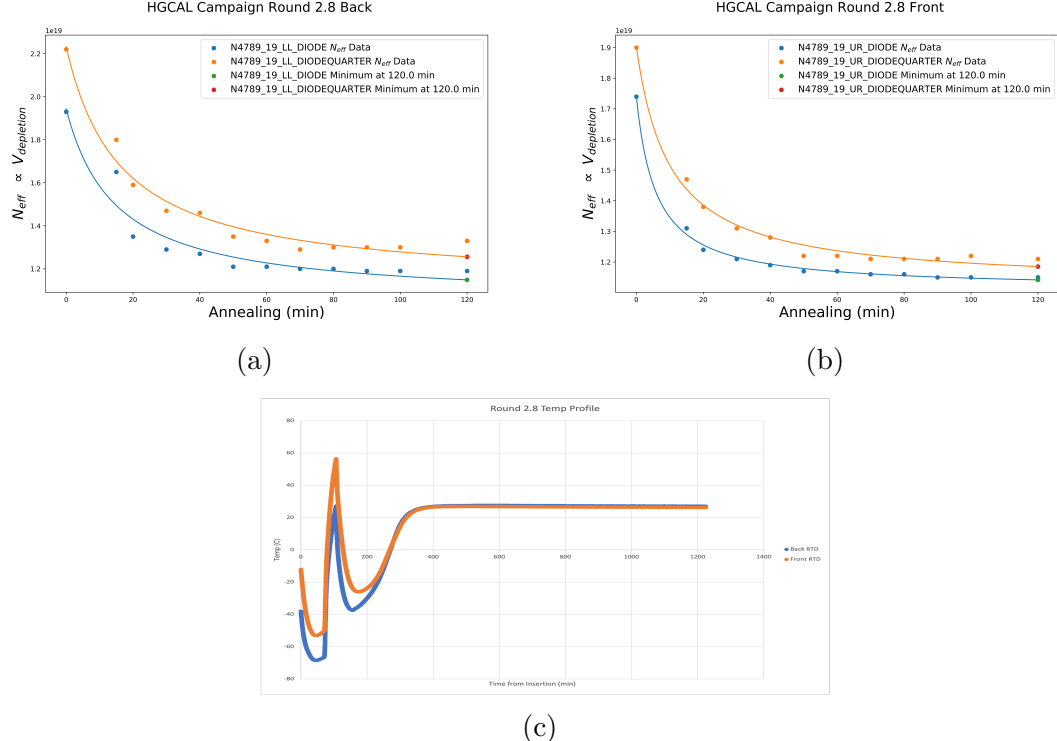


Figure 7.8: Hamburg analysis of HGCAL diodes irradiated at RINSC for 32 minutes

7.1.2 HGCAL Diodes

7.2 PIN Analysis

7.2.1 Temperature Study

7.2.2 Annealing Study

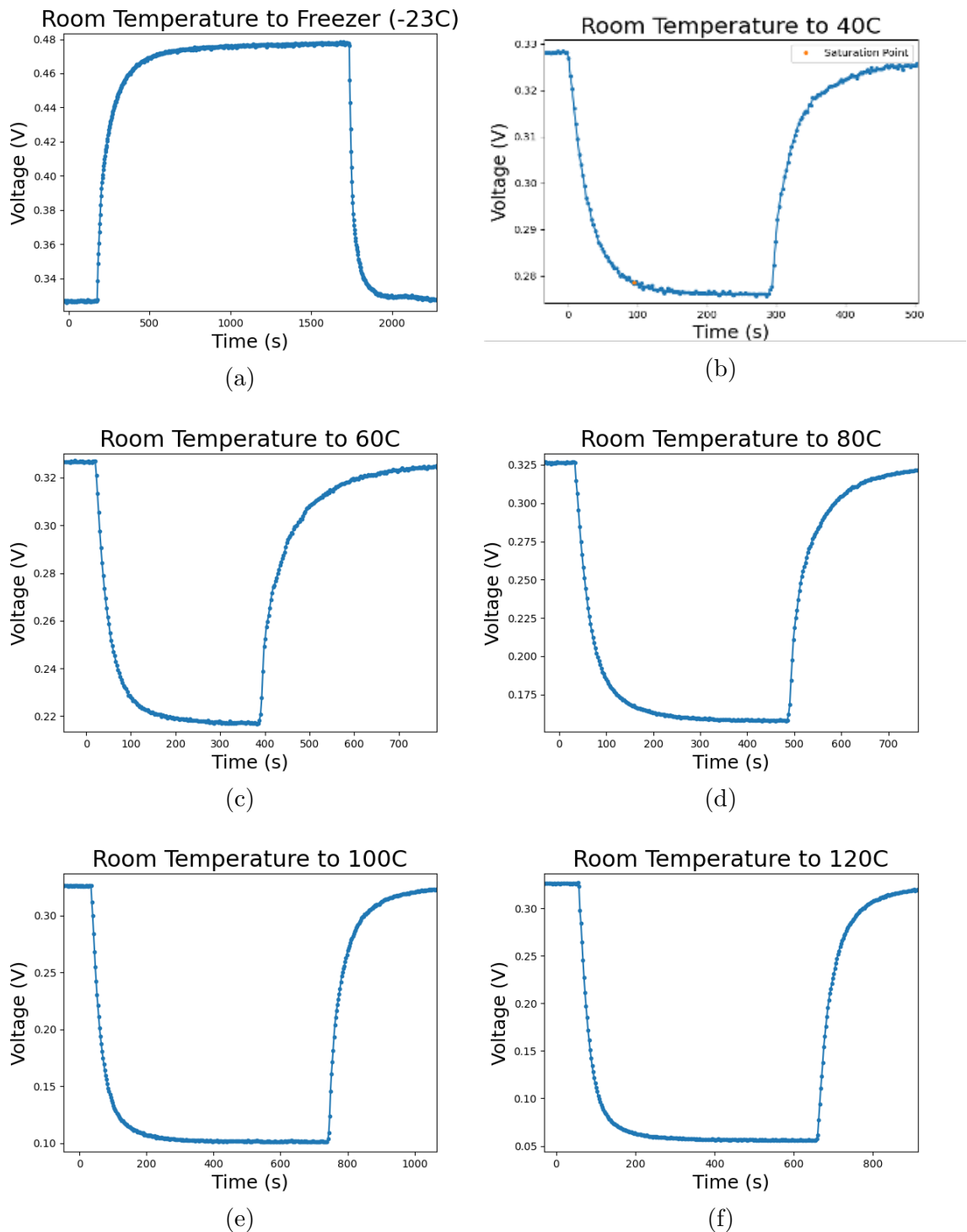


Figure 7.9: Calculated the time it took for the PIN diode to reach 95% of its saturation voltage

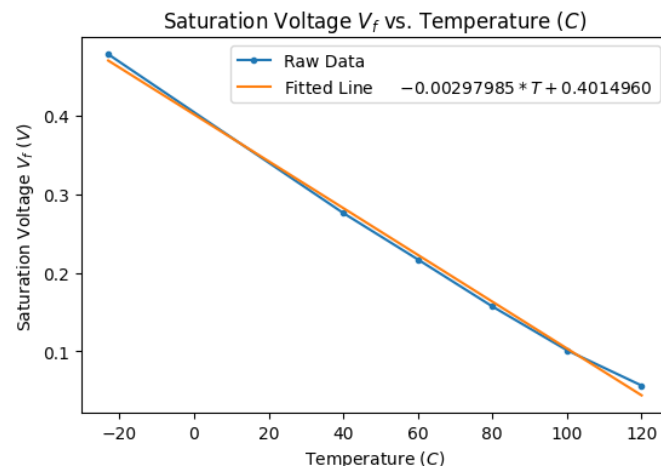


Figure 7.10: Result of PIN-thermometer analysis, found that ramp-up-time would significantly affect cumulative annealing time for short-duration annealing

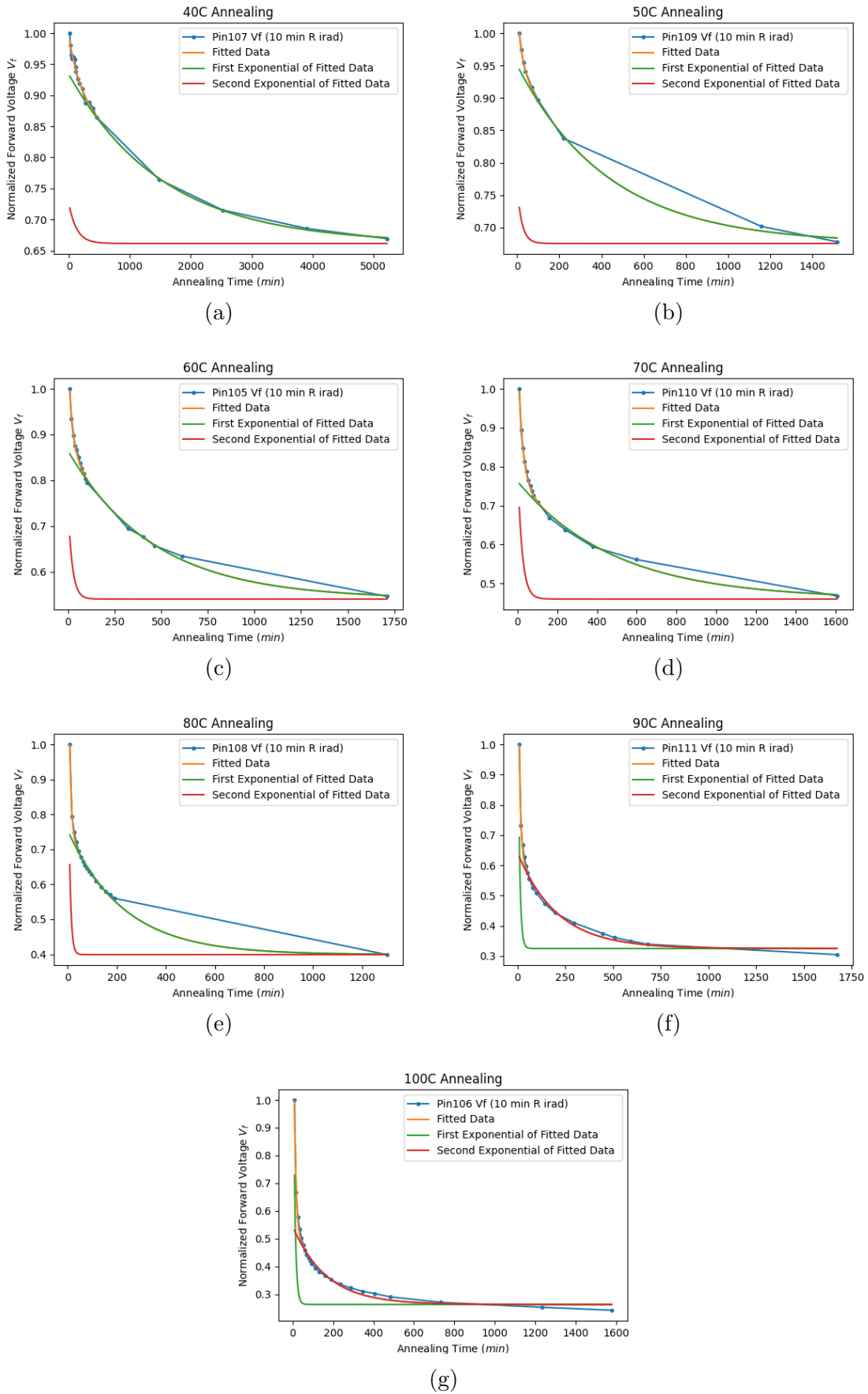


Figure 7.11: Normalized forward voltage (V_f) vs. cumulative annealing time for PIN-diodes

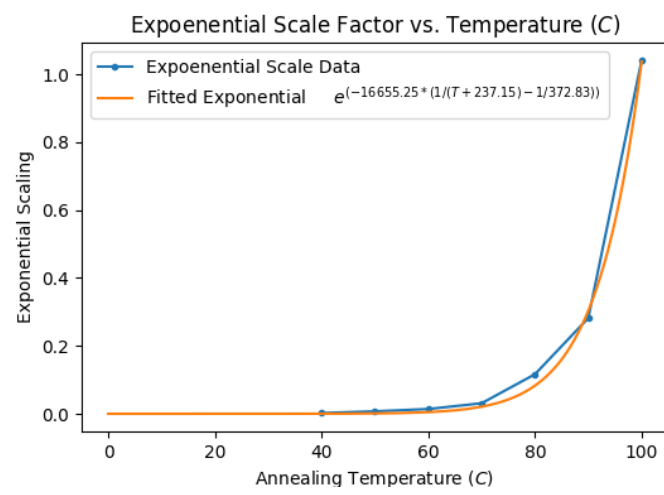


Figure 7.12: Exponential scale factor vs. temperature for PIN diodes

Chapter 8

Conclusions

8.1 Effects of Concurrent Annealing and Irradiation

8.2 RINSC-Ljubjana Cross Calibration

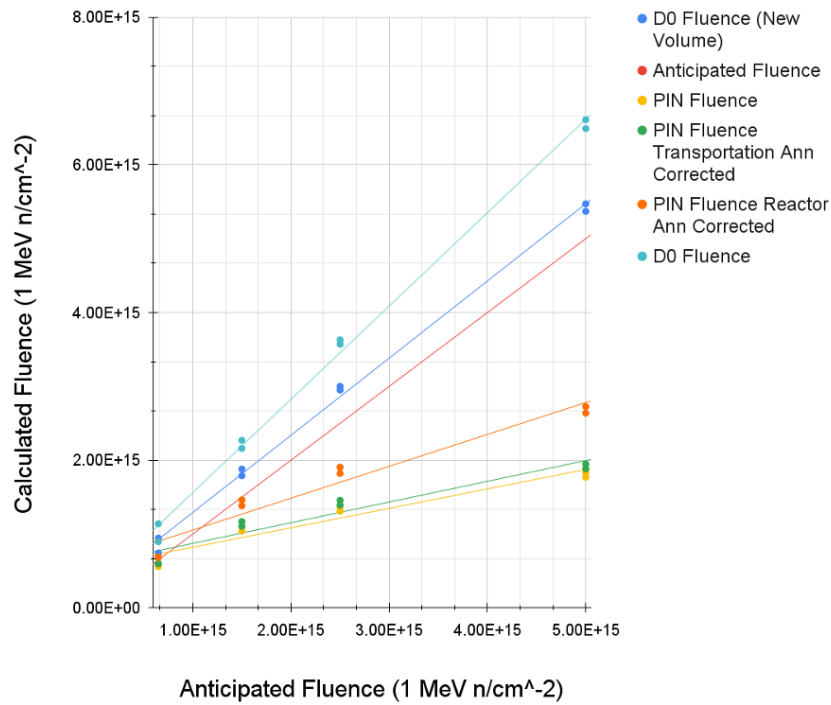


Figure 8.1: Calculated fluence of PIN and D0 diodes vs. Ljubjana anticipated values

In figure 8.1 we can see the initial D0 fluence estimate in light blue, which is far above the estimate given to us by Ljubjana. From here we investigated further and found that our value for the volume of the diode was off which lead to our fluence

estimate for the D0 diodes indicated by the blue line. This we found to be within the error and so felt we had achieved agreement with the fluence results of Ljubjana.

Bibliography

- [1] W. Adam et al. ‘P-Type Silicon Strip Sensors for the new CMS Tracker at HL-LHC’. In: *Journal of Instrumentation* 12.06 (June 2017), P06018–P06018. doi: [10.1088/1748-0221/12/06/p06018](https://doi.org/10.1088/1748-0221/12/06/p06018). URL: <https://doi.org/10.1088/1748-0221/12/06/p06018>.
- [2] Adundovi. *A P-N Junction in Thermal Equilibrium*. URL: https://en.wikipedia.org/wiki/P-N_junction.
- [3] Alexander Furgeri. ‘Quality assurance and irradiation studies on CMS silicon strip sensors’. PhD thesis. Karlsruhe U., 2006.
- [4] Julie Haffner. ‘The CERN accelerator complex. Complexe des accélérateurs du CERN’. In: (Oct. 2013). General Photo. URL: <https://cds.cern.ch/record/1621894>.
- [5] M.R. Hoeferkamp et al. ‘Application of p-i-n photodiodes to charged particle fluence measurements beyond 10^{15} 1-MeV-neutron-equivalent/cm²’. In: *Nuclear Instruments and Methods in Physics Research Section A: Accelerators, Spectrometers, Detectors and Associated Equipment* 890 (2018), pp. 108–111. ISSN: 0168-9002. doi: <https://doi.org/10.1016/j.nima.2018.02.070>. URL: <https://www.sciencedirect.com/science/article/pii/S0168900218302249>.
- [6] Gerhard Lutz. *Semiconductor Radiation Detectors*. Berlin: Springer, 1999. URL: <https://cds.cern.ch/record/887388>.
- [7] Marius Metzler. ‘Irradiation studies on n-in-p silicon strip sensors in the course of the CMS Phase-2 Outer Tracker Upgrade’. PhD thesis. Karlsruhe Institute of Technology (KIT), 2020.
- [8] Michael Moll. ‘Displacement Damage in Silicon Detectors for High Energy Physics’. In: *IEEE Transactions on Nuclear Science* 65.8 (2018), pp. 1561–1582. doi: [10.1109/TNS.2018.2819506](https://doi.org/10.1109/TNS.2018.2819506).

- [9] Michael Moll. ‘Radiation damage in silicon particle detectors: Microscopic defects and macroscopic properties’. PhD thesis. Hamburg U., 1999.
- [10] Jason Röhr. ‘Electron Transport in Solution Processed Antimony Sulphide Thin Films made from a Xanthate Precursor’. PhD thesis. Sept. 2014. DOI: [10.13140/RG.2.2.29530.39366](https://doi.org/10.13140/RG.2.2.29530.39366).
- [11] Leonardo Rossi et al. *Pixel detectors: from fundamentals to applications*. Particle acceleration and detection. Berlin: Springer, 2006. DOI: [10.1007/3-540-28333-1](https://doi.org/10.1007/3-540-28333-1). URL: <https://cds.cern.ch/record/976471>.
- [12] Tai Sakuma. ‘Cutaway diagrams of CMS detector’. In: (May 2019). URL: <https://cds.cern.ch/record/2665537>.
- [13] *Silicon Pixels Sensors at CMS*. URL: <https://home.cern/science/accelerators/large-hadron-collider>.
- [14] *The High-Luminosity large Hadron Collider*. URL: <https://home.cern/resources/faqs/high-luminosity-lhc>.
- [15] *The Large Hadron Collider*. URL: <https://home.cern/science/accelerators/large-hadron-collider>.
- [16] V A.J Van Lint et al. ‘Mechanisms of radiation effects in electronic materials. Vol. 1’. In: (Jan. 1980). URL: <https://www.osti.gov/biblio/6854931>.
- [17] Pascal Vanlaer et al. ‘The Phase-2 Upgrade of the CMS Tracker’. In: 2017.
- [18] Renate Wunstorf. ‘Systematische Untersuchungen zur Strahlenresistenz von Silizium-Detektoren für die Verwendung in Hochenergiephysik-Experimenten’. University of Hamburg, Diss., 1992. Dr. Hamburg: University of Hamburg, 1992. URL: <https://bib-pubdb1.desy.de/record/153817>.

Appendix A

Code and Data Location

1. GitHub CMS Folder:

https://github.com/AndrewTKent/CERN_CMS_Silicon_Sensor

2. Annealing Temperature Conversion:

https://github.com/AndrewTKent/CERN_CMS_Silicon_Sensor/tree/main/Diodes/DZero/Annealing_Conversion

3. HGCAL Hamburg Analysis:

https://github.com/AndrewTKent/CERN_CMS_Silicon_Sensor/tree/main/Diodes/HGCAL/Hamburg_Analysis

4. Alibava Annealing Studies:

https://github.com/AndrewTKent/CERN_CMS_Silicon_Sensor/tree/main/Diodes/Halfmoon/Annealing

5. Ljubljana vs. Rinsc Analysis:

https://github.com/AndrewTKent/CERN_CMS_Silicon_Sensor/tree/main/Diodes/Ljubljana_Diodes

6. Pin Diodes:

https://github.com/AndrewTKent/CERN_CMS_Silicon_Sensor/tree/main/Diodes/Pins